High-pressure EPR study of the calcite-CaCO$_3$(II) displacive phase transformation near 1.6 GPa

J. Dean Barnett, H. Mark Nelson, and Som Dev Tyagi*
Department of Physics and Astronomy, Brigham Young University, Provo, Utah 84602
(Received 13 April 1984)

Single-crystal EPR data have been obtained and interpreted for a Mn^{2+} ion at pressures above the calcite-CaCO$_3$(II) displacive phase transition near 1.6 GPa. In the CaCO$_3$(II) phase the Mn^{2+} ion (substitutional for Ca) sits at a point with point-group symmetry of 1 (no symmetry). The $B_{20}O_{20}$ and $B_{22}O_{22}$ terms dominate the spin Hamiltonian and allow one to define for the crystal field an effective principal axis which is not along any of the crystal-lattice directions. The data can be fit using a spin Hamiltonian of the form $\mathscr{H} = (\mathbf{H} \cdot \overleftrightarrow{\mathbf{g}} \cdot \mathbf{S}) + A\mathbf{I} \cdot \mathbf{S} + B_{20}O_{20} + B_{22}O_{22} + B_{40}O_{40} + B'_{43}O'_{43}$, where the $B'_{43}O'_{43}$ term is referred to the original calcite-site coordinate axes, and the unprimed terms are referred to the reoriented effective principal axes of the site. The new effective axes are rotated by Eulerian angles of (30°, + 17°, 30°) from the original calcite lattice axis. At 25 °C and 1.80 GPa, $B_{20} = 31.4 \pm 0.2 \times 10^{-4}$ cm^{-1} and $B_{22} = 36.0 \pm 0.5 \times 10^{-4}$ cm^{-1}, compared to $B_{20} = 25.3 \pm 0.2 \times 10^{-4}$ cm^{-1} and $B_{22} = 0$ in calcite. The values of B_{20}, B_{22}, and the Eulerian angle θ ($\simeq 17°$) vary significantly with pressure in the CaCO$_3$(II) phase.

I. INTRODUCTION

The pressure-induced, displacive, structural transformation in calcite to CaCO$_3$(II) at approximately 1.6 GPa and room temperature is of interest not only because of its geological implications but also in a fundamental physics sense as an example of a class of transformations similar to those in perovskite materials. Our primary objective in this study is the elucidation and characterization of the transformation from a microscopic viewpoint. We will not address the implications to geology.

The calcite-CaCO$_3$(II) transformation was first detected by Bridgman[1] in 1939 as a volumetric discontinuity. Interest was generated in the transformation when Van Valkenburg[2] visually observed the transformation proceed by observing a Becke line (a line dividing materials of two different indices of refraction) move across a single crystal as pressure was increased. The single-crystal to single-crystal nature of the transformation implied the displacive nature of the transformation and suggested a close relationship between the two crystal structures.

In 1975 Merrill and Bassett[3] made high-pressure, *in situ*, single-crystal, x-ray diffraction measurements on CaCO$_3$(II) and reported positional parameters for all atoms in a monoclinic $P2_1/C$ space group. They suggested a simple mechanistic atomic view of the transformation in which alternate rows of carbonate groups in each layer of the calcite structure rotate in opposite directions as described below and illustrated in Fig. 1. The x-ray work also indicated a doubling of the unit-cell volume relative to the $R\bar{3}C$ rhombohedral calcite cell. In a later work Merrill[4] proposed the identification of a zone-boundary soft mode in the calcite $R\bar{3}C$ structure at the F point of the rhombohedral Brillouin zone. One thus sees a similarity in both the mechanism and the zone-boundary character between calcite-CaCO$_3$(II) transition and the classical SrTiO$_3$ transition at 104 K and $p = 0$.

Most of the pioneering work which led to the under-standing of soft modes and related microscopic mechanisms associated with perovskite displacive transformation was carried out on materials in which the high-symmetry phase has a cubic structure and the low-symmetry phase is tetragonal or rhombohedral—specifically BaTiO$_3$, SrTiO$_3$, and closely related materials. Applications have also been made to unidirectional ferroelectrics and other soft-mode transformations which transform from tetragonal to orthorhombic structures. The calcite-CaCO$_3$(II) transformation represents an example of a soft-mode driven, zone-boundary transformation from a trigonal nonsymmorphic space group to a monoclinic crystal class. Furthermore, the structure is simple enough for one to visualize a microscopic mechanism similar in nature (but distinct in detail) to the previously studied soft-mode transformations. This work thus represents an extension of previous experimental studies to a more complex system involving two nonsymmorphic space groups with unidirectional features and low local point symmetries but still simple enough for one to analyze from a fundamental standpoint.

The high precision of the EPR technique in observing the symmetry break associated with phase transformations has been demonstrated specifically by Müller et al.[5,6] Such studies have been particularly significant when applied to continuous phase transformation, related critical phenomena, and critical fluctuations. We did not anticipate the application of EPR to critical behavior at the beginning of this study; however, variations of resonant line positions in CaCO$_3$(II) with pressure and later also some limited data at elevated temperature indicate critical phenomena do occur in CaCO$_3$. These data very strongly suggest the existence of a critical point of some nature near 200 °C and 1.5 GPa and perhaps a continuous transformation from the calcite to the CaCO$_3$(II) phase at temperatures above 200 °C. The temperature data and associated analyses will be reported in a later publication. Thus, the present study is the forerunner of a
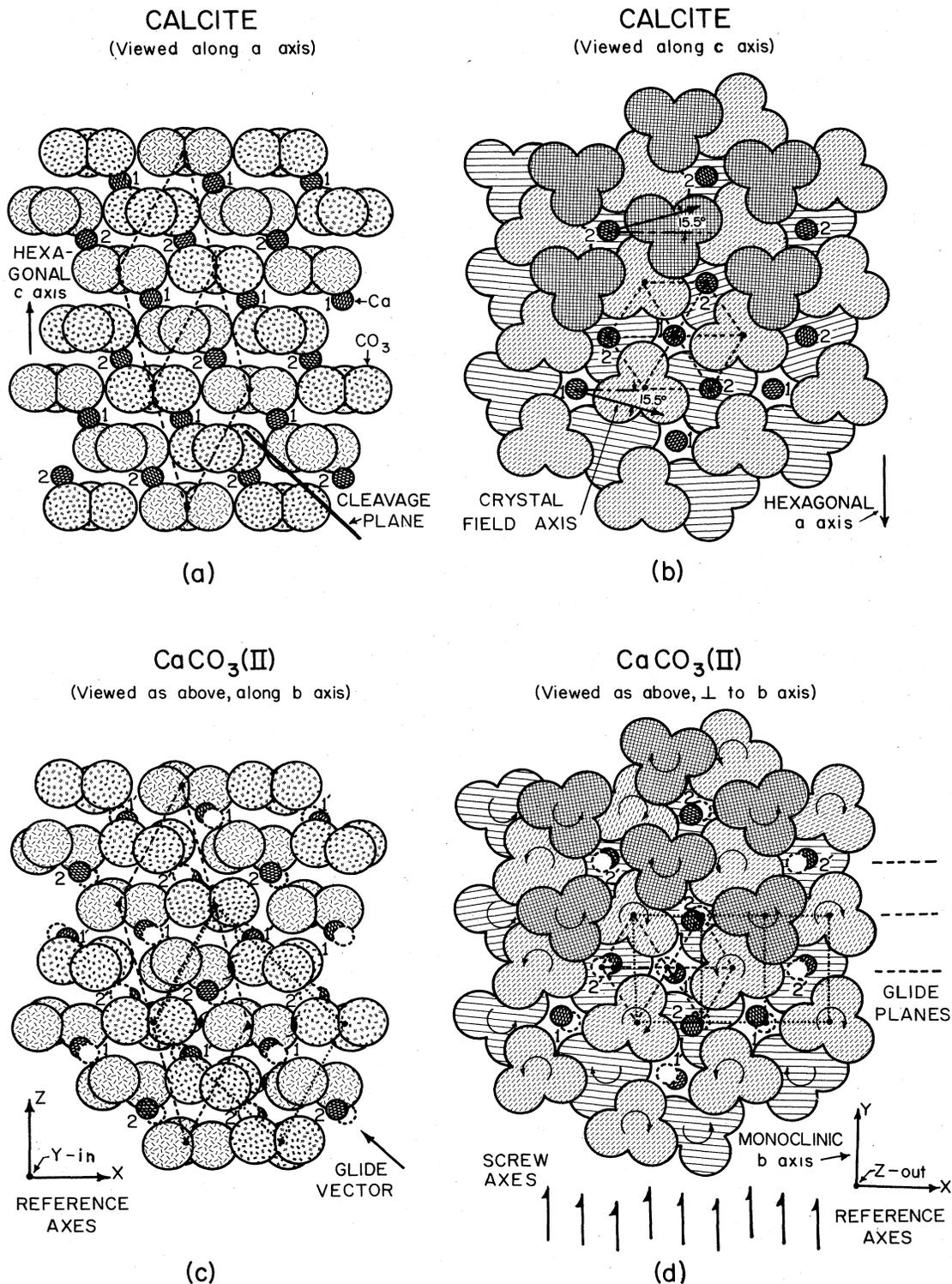
CALCITE
(Viewed along a axis)

CALCITE
(Viewed along c axis)

(a)

(b)

CaCO₃(II)
(Viewed as above, along b axis)

CaCO₃(II)
(Viewed as above, ⊥ to b axis)

(c)

(d)

FIG. 1. (a) and (b): calcite structure as viewed along the hexagonal a and c axes, respectively. (c) and (d): the CaCO₃(II) structures viewed in the same two directions following the transformation. The rhombohedral and monoclinic unit cells are shown for comparison. Note, (c) is viewed along the monoclinic b axis of CaCO₃(II). (b) and (d) specifically illustrate the symmetry of the two different Ca sites in the calcite and the four different Ca sites in CaCO₃(II), where the Mn²⁺ ion rests. Pertinent screw axes and glide planes which provide the relationships between the sites are shown. The orientations of the crystal-field principal x axes for the sites in calcite are shown in (b) and the reference Cartesian axes used to describe the orientation of the crystal-field principal directions for CaCO₃(II) are given in (c) and (d). A calcite cleavage plane is shown in (a) to uniquely define the reference axes for a physical sample.

more precise EPR study, for which we are currently constructing an apparatus with high-precision controlled pressure and temperature capabilities in order to approach the critical point more systematically. The possibility that the $CaCO_3$ crystal is thermodynamically near a critical point is an aid to one's thinking as the data and the analysis presented here are considered.

The major thrust of the work reported now is the interpretation of the $CaCO_3$(II) EPR resonant-line pattern, the formulation of a spin Hamiltonian for a Mn^{2+} ion located at the calcium site in this structure, and the elucidation of the local symmetry breaking associated with the transformation as monitored by the Mn^{2+} probe.

II. CORRELATION OF EPR DATA WITH CRYSTAL STRUCTURE FOR CALCITE AND CaCO₃(II)

In order to interpret the EPR data for $CaCO_3$(II) and to understand meaningfully the changes associated with the transformation, it is important to understand both the calcite and the $CaCO_3$(II) structures as well as the calcite EPR pattern and spin Hamiltonian.

A. Structure of calcite and CaCO₃(II)

The calcite structure can be viewed as a set of planes of carbonate groups in nearly close-packed arrangement with the calcium located in appropriate interstitial sites, as illustrated in Figs. 1(a) and 1(b). The $CaCO_3$(II) structure is illustrated in Figs. 1(c) and 1(d). Figure 1(a) shows the Ca and CO_3 ions in two consecutive planes containing the c axis as viewed along the hexagonal a (or rhombohedral $a_2 - a_3$) direction. The darker shaded CO_3 groups in Fig. 1(a) are a distance a/2 in front of the lighter shaded groups along with the corresponding calcium atoms in the same planes. Three carbonate layers perpendicular to the trigonal axis are shown in Figs. 1(b) and 1(d) so one can visualize the symmetry and nature of the sites occupied by the Ca (Mn^{2+}) ions. In order to illustrate the atomic displacements associated with the transformation to $CaCO_3$(II), the Ca atoms are shown as solid black circles, and their locations in the calcite structure are illustrated by open circles in Figs. 1(c) and 1(d). Calcite is a trigonal crystal with a rhombohedral ($R\overline{3}C$) lattice, but it is customarily referred to as a hexagonal lattice. Both the rhombohedral and monoclinic unit cells with their translation vectors and a few pertinent screw axes and glide planes are shown in Fig. 1 to show the correspondence between the two lattices and some important site symmetries. A reference Cartesian basis for later description of the crystal field is also given.

As described by Merrill and Bassett,[3] the essential features of the $CaCO_3$(II) structure can be obtained mechanistically by an ordered rotation of the CO_3 groups in calcite around the trigonal axis. The space group also allows a slight tilt. CO_3 groups in rows along the hexagonal a direction are rotated and tilted in opposite directions in alternate rows as illustrated in Figs. 1(c) and 1(d). The direction of the tilt is defined by the space group to be as shown in the figure. The direction of this unique a axis defines the unique b axis of the monoclinic cell in

$CaCO_3$(II). Rotations of the CO_3 groups in adjacent layers are such that the a_1 rhombohedral lattice vector remains a translation vector of the monoclinic lattice. The calcium atoms are repositioned to the center of the distorted interstitial sites. All the essential symmetry features of $CaCO_3$(II) and the atomic positions obtained by this mechanism using a CO_3 rotation of 11° and a tilt of 1° are in reasonably good agreement with x-ray measured positional parameters of Merrill and Bassett.[3]

B. EPR results for calcite

There have been several previous EPR studies of Mn^{2+} ions in calcite at atmospheric pressure. The first investigation was by Hurd et al.[7] in 1954. They carefully studied the resonant-line pattern with H parallel and with H perpendicular to the trigonal axis and concluded the local site was axially symmetric relative to this axis. They observed 30 resonance lines in both these directions. They did make limited measurements at other angles and reported some splitting of lines when θ differed significantly from 0° or 90°. Using second-order perturbation theory and a Hamiltonian which included the hyperfine nuclear-spin interaction, the Zeeman term, and only cylindrically symmetric $B_{20}O_{20}$ and $B_{40}O_{40}$ in the crystalline-potential expression, Hurd et al. were able to fit their data along symmetry directions with a precision of ± 1 G. They made no attempt to explain the line splitting for nonsymmetric directions. Kikuchi[8] and McConnell[9] suggested the line splitting was a consequence of the two sites (1) and (2) shown in Fig. 1(b), which are not orientationally equivalent (related by a twofold screw axis). Barberis et al.[10] inserted the $B_{43}O_{43}$ terms in the crystalline-field potential of the Hamiltonian and obtained agreement with careful measurements of the splitting as a function of the angle ϕ around the trigonal axis. They proved that the principal axes of the crystalline field at the two Ca^{2+} sites were rotated an angle λ of $\pm 15.5°$ from the coordinate axes defined by the crystal as shown for the two sites in Fig. 1(b) [$+15.5°$ for site (1) and $+15.5°$ for site (2)].[11] This misorientation of the local crystalline fields from the crystallographic axes is a consequence of the location of the oxygen ligands relative to the Ca^{2+} site. In order to uniquely specify the orientation of the crystal-field axes in a physical sample as discussed later, we have illustrated a cleavage plane in Fig. 1(a).

For later reference we now write the calcite-Mn^{2+} spin Hamiltonian using the customary notation in terms of the electron spin S and the nuclear spin I of the manganese ion with the symmetrized spin operators O_{lm} and their associated coefficients B_{lm} (see Abragam and Bleaney[12]). Thus we have

$$\mathcal{H}_{(calcite)} = \beta(\mathbf{H} \cdot \vec{g} \cdot \mathbf{S}) + A\mathbf{I} \cdot \mathbf{S} + B_{20}O_{20}$$
$$+ B_{40}O_{40} + B_{43}O_{43} , \tag{1}$$

where for the coordinate axes we have utilized the principal axes of the crystalline field at a specific site rather than the calcite-lattice axes.

C. General EPR features for CaCO₃(II)

Knowing the EPR data for calcite and the symmetry of the two crystals from the x-ray study, we can predict the

qualitative features of the EPR pattern in the CaCO$_3$(II) phase. First, the hyperfine splitting, being a nuclear interaction, must change only very slightly. Second, because of the displacive nature of the transformation and the relatively minor rearrangement of the atoms near the Mn^{2+} ion, one expects some correlation can be made between the CaCO$_3$(II) EPR pattern and the calcite EPR pattern.

As seen in Fig. 1(d), there are four nonequivalent Ca^{2+} sites in CaCO$_3$(II), designated by (1), (1'), (2), and (2'). Sites (1) and (2), as well as (1') and (2'), are related by a glide plane (mirror) with glide vector illustrated. Sites (2) and (1'), as well as (2') and (1), are related by a twofold screw axis shown. Site (1) is related to (1') and site (2) to (2') by inversion centers. Since EPR absorption is not influenced by H field reversal, sites (1) and (1') form a single resonance pattern, which varies in a unique way with orientation of H and is designated as pattern I. Sites (2) and (2') also form a single but different resonant pattern, which has unique orientational variations and is designated as pattern II. Pattern II orientation features exhibit a mirror relationship to the orientation features of pattern I. The mirror plane experimentally identifies the monoclinic crystal mirror plane. The orientation features of patterns I and II must also be related by a twofold rotation symmetry associated with the screw axis. Since each site has a point symmetry of 1 (no symmetry), the pattern associated with a single site should exhibit no symmetry except the inversion associated with the magnetic field reversal. The principal axes of the crystalline field (to the extent they can be experimentally determined) are determined by the nonsymmetric locations of the nearby charges and are not related in any obvious way to the crystal axes.

III. EXPERIMENTAL PROCEDURE

The EPR measurements were made using the high-pressure hydrostatic EPR cell developed earlier in this laboratory.[13] This cell utilizes a cylindrical, silver-coated, solid-sapphire, resonant cavity 1.25 cm in diameter and 1.78 cm long, which also serves as an anvil in a gasketed Bridgman anvil or squeezer-type pressure apparatus. The sample chamber is a small circular volume approximately 0.2 mm thick and 1 mm in diameter, which is located at the center of one end of the cavity and communicates electromagnetically with the cavity through a hole cut in the silver coating of the cavity. Microwave energy is capacitively coupled to the cavity itself through an opening in the silver coating at the opposite end of the cavity. A standard Varian model No. V-4500 EPR X-band spectrometer using 100-kHz modulation is utilized to record the EPR derivative spectra. The cavity has a Q of approximately 2500 for the TM$_{110}$ mode used. Samples with 10^{14} spins can be studied without difficulty. Although the Q is less than for a standard air cavity, the filling factor is larger. As a result, the sensitivity of the pressure cavity is actually greater than that of the commercial air cavity provided with the instrument. There is no degradation of the EPR pattern at higher pressures since the pressures are hydrostatic. One serious limitation of the high-pressure EPR cell is its limited orientational freedom. To change the direction of the magnetic field, the total pres-

sure cell, including the cavity and the modulation coils, is rotated in the magnetic field. A change in orientation of 45° from the optimum orientation seriously decreases the signal strength and limits effective data collection to ±45° from a preselected direction.

By including a small chip of ruby in each sample as a pressure sensor, pressures are measured using the ruby fluorescence technique[14] to a precision of ±0.3 GPa, as described in our EPR apparatus paper.[13] The potential overlapping of the EPR patterns of the ruby and the CaCO$_3$ was a concern, but by keeping the size of the ruby small relative to the sample (between $\frac{1}{10}$ and $\frac{1}{50}$ in volume), the ruby lines were seldom observable.

The calcite samples with Mn^{2+} impurities were of geological origin, and samples with higher impurity concentrations were selected to increase the EPR signal. Since in CaCO$_3$(II) only 50% of the Mn^{2+} ions are in sites which simultaneously resonate, the EPR signal amplitude in the CaCO$_3$(II) phase was approximately half that of the resonance lines in calcite. No attempt was made to determine the precise Mn^{2+} concentration. Comparison with previous EPR work was felt to be adequate to characterize the sample. Samples were cut with a rotary saw into thin sheets approximately 0.5 mm thick such that the trigonal axis was either perpendicular or parallel to the sheet. By using lapidary techniques, the sheets were ground to an approximate thickness of 0.2 mm and were then polished. Under a microscope, sections of an appropriate dimension to fit into the sample chamber were obtained by cleavage of this thin sheet into irregular planar pieces.

There are three possible orientations of the monoclinic CaCO$_3$(II) axes relative to the trigonal calcite axes. When passing through the calcite → CaCO$_3$(II) transition, one must avoid multiple nucleation by applying pressure slowly in order to preserve the single-crystal feature in the CaCO$_3$(II) phase. During the course of this investigation, we have taken approximately twenty samples with planar dimensions between 0.5 and 0.8 mm through this transformation, and on only two or three occasions have we failed to obtain a single crystal in the CaCO$_3$(II) phase. Several samples have been repeatedly taken back and forth through the transition. This sample reversal in perovskite structures is common, but the volume changes involved are generally less than 0.1%; whereas, in calcite the volume change is ten times greater, and more care must be exercised. The nucleation and growth of the CaCO$_3$(II) phase does, however, yield a monodomain sample, which is often difficult to obtain in the perovskites.

Each sample was placed in the pressure chamber, and a preliminary EPR orientational study was made to locate precisely the calcite-lattice orientation. All features of the CaCO$_3$(II) EPR pattern from many samples could then be referenced to the calcite coordinate system. Since the EPR goniometer has orientational flexibility of only ±45° in any direction and since the experimenter has no control over which of the three orientations the monoclinic CaCO$_3$(II) axis will take, several different samples were used, and variations in the pattern over all values of the orientational angles were pieced together by comparing overlapping regions.

In a particular experiment pressure is applied at a

reasonably fast rate up to a pressure close but definitely below the transformation, and then pressure is increased slowly to avoid multiple nucleation. The actual point of transformation can be easily detected by setting the magnetic field on a line of reasonably intensity and slowly increasing pressure. As the transformation proceeds, the line intensity decreases slowly or rapidly depending on the rate of pressure increase, and a totally new EPR pattern appears.

IV. EXPERIMENTAL DATA

Upon passing through the transformation at room temperature and approximately 1.6 GPa, some of the qualitative aspects of the $CaCO_3(II)$ data mentioned in Sec. II C are apparent. A 60-line pattern exists. The hyperfine interaction is only slightly changed. The $M = \frac{1}{2}$ to $M = -\frac{1}{2}$ lines, which are orientationally insensitive in calcite, are slightly doubled and readily identifiable, but all other lines are so scrambled that no obvious identification is apparent.

A. Determination of crystal-field-site axes

Orientational searches readily identify a mirror plane and the two independent sets of resonance lines which are associated with the two sets of sites [2 with (2') and 1 with (1')]. Concentrating on the lines associated with one of two distinct sites, we found three resonance-field extrema and measured their orientation relative to the calcite-lattice reference frame to within a precision of approximately $\pm 1°$ in any direction. The orientational angles so measured were recognized to be consistent with an orthogonal set of basis vectors to within the precision of the measurements. The crystal field at a site which has a point-group symmetry of 1 does not technically have a principal axis, but since in this case the $B_{20}O_{20}$ and $B_{22}O_{22}$ terms totally dominate the Hamiltonian, extremal orientations establish an orthogonal basis associated with these terms. It is, therefore, meaningful to experimentally define basis vectors associated strictly with these two terms. Figure 2 illustrates the set of basis vectors for each site so defined and measured relative to the calcite crystal axes shown in Fig. 1. We note that there is no way to determine experimentally which site accompanies which set of EPR lines. Calculations of the local potential functions based on a point-charge model have allowed us to make this determination, and we have labeled each set of axes (1 and 1') or (2 and 2') in Fig. 2 with a subscript corresponding to the label of that particular site in Figs. 1(c) and 1(d).

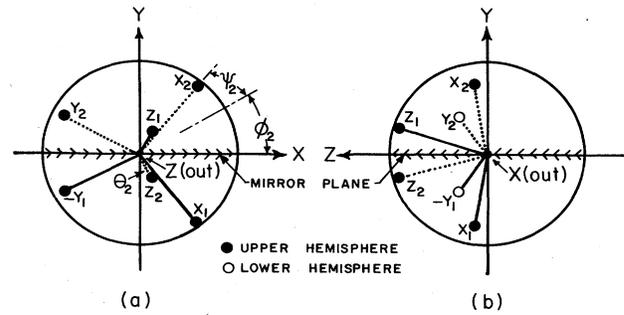With the right-handed Cartesian axis placed on Fig. 1

FIG. 2. Two orthogonal stereographic projections of the measured crystal-field effective principal axes for the two sets of sites (1 and 1') and (2 and 2'). The reference axes are the axes shown in Fig. 1, and the subscripts correspond to the site designations there. The Eulerian angles (ϕ, θ, ψ) required to obtain site (2) are also illustrated in (a).

as reference, the angular coordinates for the basis vectors for site (2) are given in Table I, where β is the polar angle measured from the z axis and α is the azimuthal angle measured from the x axis. The orientation of these axes can be obtained by Eulerian rotations of the reference axes of the form $(-30°, -17°, -30°)$ for site (1), and $(+30°, +17°, +30°)$ for site (2). The calculated angular coordinates based on these Eulerian angles are shown for the axes of site (2) for comparison with the actual measured directions in Table I. The orientation of the z axis is the most easily measured with precision since both z_1 and z_2, as well as the reference z from calcite, can be measured on a single sample within the $\pm 45°$ orientational limitation of the pressure cell. Repeated measurements indicate the α values for the z_1 and z_2 axes are separated by $120° \pm 1°$. The β values of the two z axes, shown as $17°$ in Fig. 2, were observed to vary measurably (approximately $5°$ per GPa) between 1.6 and 2.0 GPa.

To avoid ambiguity when describing the orientation of the crystal-field axes in both calcite and $CaCO_3(II)$, one must exercise care to assign the same reference coordinate axes for recording data from an experimental sample and for use with the associated analytical spin-Hamiltonian formulation. Since calcite does not exhibit a mirror plane perpendicular to the c axis, two different orientational states will have their c axes and their a axes along common lines, respectively. To uniquely define the orientation of a crystal relative to a set of reference axes, one must specify the positive sense of each axis and then distinguish between the two possible orientational states of the crystal. The specification of a cleavage plane relative to coordinate axes will uniquely attach the axes to the

TABLE I. Comparison of basis vector orientations for site (2) from experiment and those based on an Eulerian rotation of $(+30°, +17°, +30°)$.

Basis vector	Experimental		Assumed Eulerian rotation	
	Polar angle β	Azimuthal angle α	Polar angle β	Azimuthal angle α
x_2	81°	60°	81.6°	58.9°
y_2	75°	152°	75.3°	151.1°
z_2	17°	−60°	17°	−60°

crystal sample. The axes used to describe a microscopic model must then be consistent with these axes attached to the sample. The variations of the resonance-line positions as well as the mathematical formalism of the spin Hamiltonian are then referred to the same set of axes.

To avoid any possible ambiguity, we have placed reference axes on Fig. 1 and have shown a cleavage plane on the drawing. All data and all analysis are referred to these axes. We have also illustrated in Fig. 1(b) the orientation of the spin-Hamiltonian principal x axes for the two Ca sites in calcite. We have used the same reference axes in Fig. 2 to describe the orientation of the crystal-field axes for $CaCO_3(II)$. Barberis *et al.*[10] did not report their data in sufficient detail to avoid this ambiguity.

B. Correspondence of $CaCO_3(II)$ and calcite resonance-line positions

As is common in EPR studies, careful measurements were made with **H** along each of the three symmetry axes of the site itself. Figure 3 illustrates the comparison of experimental results at room temperature between the calcite pattern with **H** parallel and with **H** perpendicular to the hexagonal c axis and the $CaCO_3(II)$ pattern with **H** parallel to the z_2 and y_2 directions for a single site. Some resonance lines (shown dashed in Fig. 3) were not measurable due to serious overlapping, often with lines associated with the other site. In the x_2 (or x_1) direction the line shifts due to the fine-structure terms are less than 50 G for all lines; therefore, extensive overlapping of lines exists. Measurements were taken with **H** parallel to the x_2 (or x_1) direction and at orientations near this axis to determine its orientation, but precise line positions were not attempted. In contrast to the insensitivity of the calcite pattern to pressure, there was a very sizable shift of the lines with pressure in the $CaCO_3(II)$ phase. For example, the largest shift of any calcite line as pressure is increased from atmospheric pressure to 1.5 GPa is 4 G, whereas some $CaCO_3(II)$ lines shift approximately 200 G/GPa above the transition.

With **H** along the appropriate principal axes, one can see rather easily the correspondence of the lines in the $CaCO_3(II)$ pattern to lines in the calcite pattern, as illustrated in Fig. 3. The data points shown in Fig. 3 had uncertainties less than the width of the lines on the drawing. In both of the directions shown, measurements were taken at several pressures as indicated by the arrows placed along the pressure axis. Note that the measurements in the two directions were not taken at the same pressures. For careful fitting of a spin Hamiltonian, linear interpolation and extrapolation were used to obtain resonance-line positions in the two directions at 1.8 and 2.0 GPa. Observed line positions in two principle directions at 1.8 GPa obtained with a microwave-cavity frequency of 8.955 GHz are given in Table II along with calculated line positions from the spin Hamiltonian for comparison. The spin-Hamiltonian parameters determined for $CaCO_3(II)$ at both 1.8 and 2.0 GPa as well as the parameters for calcite at atmospheric pressure are given in Table III.

V. SPIN HAMILTONIAN FOR CaCO₃(II)

The dominant difference between the crystal field in calcite and the rotated crystal field in $CaCO_3(II)$ is the inclusion of a $B_{22}O_{22}$ term in the Hamiltonian. Using only the $B_{20}O_{20}$, $B_{40}O_{40}$, and this additional $B_{22}O_{22}$ term, one can obtain agreement of all lines in the two patterns (z_2 and y_2 directions) to a maximum discrepancy of 25 G at both pressures. In order to reduce this discrepancy, other possible terms were considered. If referred to the same axis as the dominant terms, the $B_{43}O_{43}$ term cannot make any contribution in the z_2 and y_2 directions since it gives only a second-order correction in the y and z directions. Furthermore, terms of the type $B_{42}O_{42}$, $B_{44}O_{44}$ would attribute to the site a true Cartesian symmetry, which is not really expected. In order to achieve completeness, fits us-
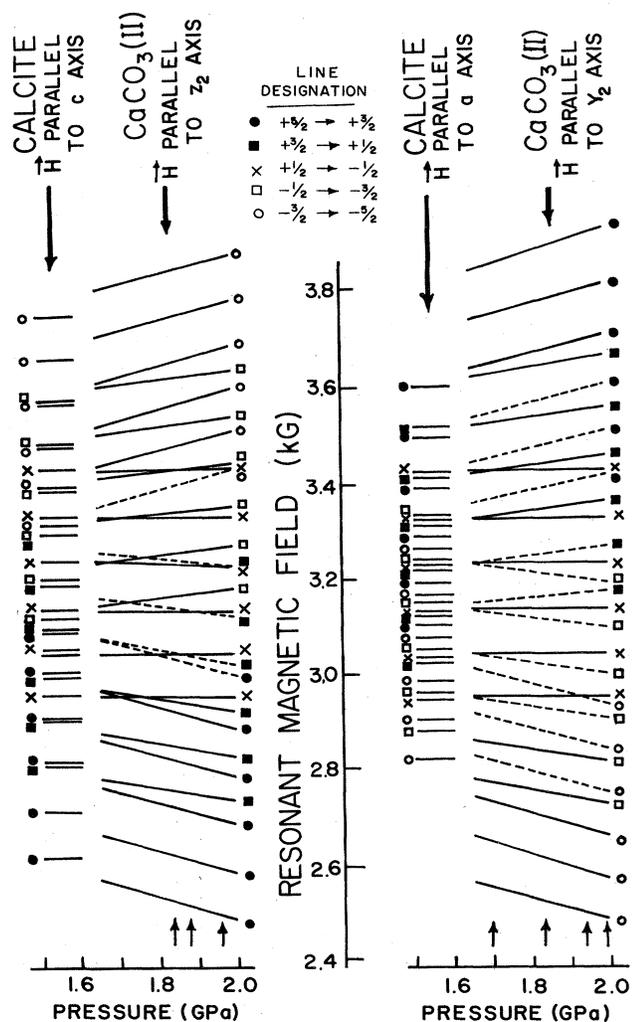

FIG. 3. Comparison of the observed EPR patterns in calcite below the phase transition and a single site for $CaCO_3(II)$ above the transition. The comparison is for directions along the site-effective principal axes for both calcite and $CaCO_3(II)$ where the correspondence is most apparent. Measurements were made at the pressures indicated by the arrows along the pressure axis.

TABLE II. Experimental and calculated EPR line positions in $CaCO_3(II)$ at 1.8-GPa pressure and room temperature.

Transition		H parallel to z_2 axis			H parallel to y_2 axis		
M	m	H_{expt} (G)	H_{cal} (G)	ΔH (G)	H_{expt} (G)	H_{cal} (G)	ΔH (G)
$+\frac{5}{2}$	$+\frac{5}{2}$	2531	2530	$+1$		3383	
	$+\frac{3}{2}$	2626	2627	-1		3474	
	$+\frac{1}{2}$	2727	2725	$+2$		3569	
	$-\frac{1}{2}$	2824	2826	-2	3667	3669	-2
	$-\frac{3}{2}$	2927	2930	-3	3774	3772	$+2$
	$-\frac{5}{2}$		3037		3882	3880	$+2$
$+\frac{3}{2}$	$+\frac{5}{2}$	2757	2752	$+5$		3160	
	$+\frac{3}{2}$	2849	2844	$+5$		3250	
	$+\frac{1}{2}$	2943	2940	$+3$	3344	3342	$+2$
	$-\frac{1}{2}$		3038		3443	3438	$+5$
	$-\frac{3}{2}$		3139		3538	3538	0
	$-\frac{5}{2}$		3243		3639	3639	0
$+\frac{1}{2}$	$+\frac{5}{2}$	2948	2947	$+1$	2948	2955	-7
	$+\frac{3}{2}$	3038	3037	$+1$	3038	3043	-5
	$+\frac{1}{2}$	3131	3130	$+1$	3133	3134	-1
	$-\frac{1}{2}$	3227	3225	$+1$	3227	3227	0
	$-\frac{3}{2}$	3324	3323	$+1$	3324	3322	$+2$
	$-\frac{5}{2}$	3424	3424	0	3423	3420	$+3$
$-\frac{1}{2}$	$+\frac{5}{2}$	3155	3150	$+5$	2756	2755	$+1$
	$+\frac{3}{2}$	3242	3238	$+4$	2841	2843	-2
	$+\frac{1}{2}$	3330	3327	$+3$		2931	
	$-\frac{1}{2}$	3419	3420	-1		3025	
	$-\frac{3}{2}$	3512	3515	-3		3114	
	$-\frac{5}{2}$	3612	3613	-1		3208	
$-\frac{3}{2}$	$+\frac{5}{2}$		3380		2534	2534	0
	$+\frac{3}{2}$	3462	3464	-2	2623	2623	0
	$+\frac{1}{2}$	3548	3551	-1	2709	2710	-1
	$-\frac{1}{2}$	3642	3641	$+1$		2798	
	$-\frac{3}{2}$	3733	3733	-1		2888	
	$-\frac{5}{2}$	3828	3830	-2		2979	

ing terms of this type were tried but with no significant improvement. For terms of lower symmetry, one must specify their orientation as well as their magnitude; thus, several parameters are involved.

Because of the microscopic nature of the transformation and the similarity of the $CaCO_3(II)$ structure to the calcite trigonal structure, one might expect the existence of a $B_{43}O_{43}$ term oriented very nearly the same as in the original trigonal crystal. Such a term, now at a different orientation from the dominant terms, can, of course, be expressed as a series of terms of the form $\sum_{m=-4}^{+4} C_{4m}O_{4m}$ when referred to the axis of the dominant terms. This term thus reduces the symmetry of the site to point-group 1. With no more justification than that just stated and with a desire of keeping the number of free variables to a minimum, we attempted a fit including a $B_{43}O_{43}$ term oriented precisely as it was in calcite but with variable magnitude. Such an assumption produced the agreement shown in Table II, which indicates discrepancies three to four times smaller than without the

TABLE III. Comparison of the spin-Hamiltonian parameters for calcite and CaCO$_3$(II).

Parameter	Calcite $(10^{-4}$ cm$^{-1})$	CaCO$_3$(II) 1.8 GPa $(10^{-4}$ cm$^{-1})$	2.0 GPa $(10^{-4}$ cm$^{-1})$
A	87.78 ±0.08[a]	88.6±0.2	88.6±0.2
B_{20}	25.3 ±0.2[a]	31.4±0.2	34.7±0.2
B_{22}	0	36.0±0.5	39.7±0.5
B_{40}	4.0 ±0.2[a]	4.0±0.5	4.0±0.5
B'_{43}	−0.918±0.2[b]	−2.5±1.0	−2.5±1.0
g (unitless)	2.0018±0.0006[a]	2.0025±0.0006	2.0025±0.0006

[a]These values taken from Ref. 7, but B_{40} term differs by precisely a factor of 100, due to an apparent error in that paper.

[b]This value taken from the data of Ref. 10, but differs by $\sqrt{2}$ from the value reported there, due to a minor computational error in that paper. The B'_{43} coefficient could be made positive by referring it to the calcite-site axes rotated 180° from the axes given in Ref. 10 and used in this paper.

$B_{43}O_{43}$ term. As a further check, a series of patterns was taken with **H** along several directions laying in the monoclinic mirror plane at various polar angles θ from the reference z axis. The $B_{43}O_{43}$ term should be large in these directions. Agreement between experimental and calculated values was within a few gauss. We have thus concluded that the dominant shifting of the crystal field as one passes through the transformation is a tilting of the principal axis associated with the $B_{20}O_{20}$ term and the inclusion of a $B_{22}O_{22}$ term along the same axis with a residual $B'_{43}O'_{43}$ term remaining in the orientation of the original calcite reference frame. We can now write a spin Hamiltonian for CaCO$_3$(II)-Mn^{2+} as

$$\mathcal{H}_{[CaCO_3(II)]} = \beta(\mathbf{H} \cdot \overleftrightarrow{g} \cdot \mathbf{S}) + A\mathbf{I} \cdot \mathbf{S} + B_{20}O_{20}$$

$$+ B_{22}O_{22} + B_{40}O_{40} + B'_{43}O'_{43} , \quad (2)$$

where the prime implies reference to a different coordinate system as described. We realize that this approach is very unconventional, but it does allow a fitting of the data with a minimum number of parameters and provides insight into the data not obtained using a single reference axis. This approach is also consistent with our expectations of a continuous phase transition since the two sets of axes can coalesce as one approaches the transition, and the value of B_{22} can simultaneously approach zero.

It is significant that we have included, in addition to those parameters for calcite, only two new parameters, B_{22} and the tilt angle θ of the z axis. We note that both B_{22} and θ vary significantly with pressure, and there may be a possible relationship between the two. By adopting this approach we have not considered the 30° Eulerian rotation angle of the principal axes as a parameter. In Table III the spin-Hamiltonian parameters obtained from the computer fits at the two pressures are compared with those of calcite along with the expected accuracy. We note in passing that due to the lack of symmetry at the site, the $\overleftrightarrow{g}$ tensor could have a general tensor form in CaCO$_3$(II). We assumed a spherically symmetric form for $\overleftrightarrow{g}$ and found little change in $|g|$ across the transition. Details of the procedure for fitting the spin Hamiltonian given in Eq. (2) to the data are found in the Appendix.

VI. DISCUSSION AND CONCLUSIONS

The EPR pattern for CaCO$_3$(II)-Mn^{2+} has been shown to be consistent in every respect with the $P2_1/c$ structure reported by Merrill and Bassett.[3] These authors considered but rejected a space group $P2_1$ as a possible structure,[15] and we concur. The $P2_1$ space group does not have a center of symmetry; thus, each of the four sites in Fig. 1(d) would produce an independent pattern, and a 120-line EPR pattern would have been observed in at least some orientations.

We have successfully measured the EPR spectrum of the Mn^{2+} ion at a site of point symmetry 1, and, utilizing the spin-Hamiltonian formalism, we have parametrized the data with only four crystal-field terms in the potential expansion by using an unconventional technique of allowing a residual $B'_{43}O'_{43}$ in the original calcite reference axis. From the data in Table II, it is obvious that while the fitting is reasonable though not superb, the dominant effects are accounted for. Considering the mechanistic CO$_3$-group rotation-tilt model of the transformation, one might expect the $B'_{43}O'_{43}$ term in CaCO$_3$(II) to be rotated slightly from the orientation in calcite. The determination of the precise orientation of this term would require considerable effort and seems less important than the facts that (1) the term is in approximately the same orientation and (2) it remains in the expansion. Point-charge-model calculations of B'_{43} based on the atomic displacements associated with the transformation indicate small changes in the value of the B'_{43} term and approximately 2° change in its orientation. This same model predicts large values for B_{22} and large changes in B_{20}. The dominant features of the transformation, as observed by EPR, are the creation of the $B_{22}O_{22}$ term and the tilting of the pseudoprincipal axis associated with the dominant terms of the field. The solution of the eigenvalue problem through the use of a spin Hamiltonian with terms based on two different coordinate axes presented some challenge, the details of which are left to the Appendix.

Preliminary temperature-dependent data not reported here demonstrate dramatic resonant-line shift and suggest the possibility of a continuous transition between the two structures at a critical point and thus a continuous

coalescing of the crystal field of the two structures. Based on this proposition, Hatch and Merrill[16] have used group-theoretical techniques to consider the symmetry compatibility of these two structures in terms of the Landau-symmetry criteria of second-order phase transitions and have shown the two structures to be compatible for such a transition in this classical approximation. However, a more recent analysis by Felix and Hatch[17,18] using a renormalization-group analysis does not indicate the existence of a stable fixed point and, consequently, indicates the transition does not go continuously. Additional experimental and theoretical work is needed.

In this paper we have not attempted to give a microscopic explanation of the variation with pressure of either the spin-Hamiltonian parameter or the orientational angle θ in $CaCO_3(II)$; nor have we tried to explain the discontinuous shift of these parameters from the values in calcite. These variations are associated with the proposed critical phenomena at higher temperatures, and the variations are much larger and dramatic in our preliminary temperature data. We are now preparing a manuscript in which we report preliminary temperature data and use microscopic model calculations to interpret these observed variations in terms of the atomic displacements near a solid-solid critical point. The data and analysis reported here provide only the base for the later detailed study of this symmetry break using EPR techniques.

The specification of Eulerian rotation angles $(30°, \theta, 30°)$ required to obtain the experimentally observed axis orientation for sites (2) and (2') and $(-30°, -\theta, -30°)$ for sites (1) and (1') deserves some comment. The use of the precise values of 30° suggests a residual from the trigonal symmetry of calcite, for which result we have no explanation. The selection of the reference axes shown in Figs. 1 and 2 is, of course, arbitrary. We have selected these axes such that some symmetry is demonstrated between the Eulerian angles required to obtain the two different site axes. Alternate choices which also demonstrate such a symmetry could be selected. The essence of the data is that when the symmetry between the two sites is considered, the orientation of the z_2 axis (evidenced by the value of the Eulerian angle ϕ) and also the orientation of the $(x_2 - y_2)$ plane (evidenced by the value of the Eulerian angle ψ) must be specified by an angle which we commonly associate with trigonal symmetry. It is possible that these two angles have the required values by coincidence, but there are two simultaneous, seemingly independent coincidences. If only a single-order parameter is involved in the transition, such residual symmetry-related angles have no logical foundation in the group theoretical formulation. The explanation for the 30° angles may be found in the fact that the lattice is still essentially rhombohedral and since the B_{20} or B_{22} coefficients calculated from point charges require a lattice sum rather than simply nearest-neighbor terms, the lattice effects may dominate.

ACKNOWLEDGMENTS

APPENDIX

The spin Hamiltonian for $CaCO_3(II):Mn^{2+}$ is taken to be

$$\mathcal{H} = \beta(\mathbf{H} \cdot \overleftrightarrow{g} \cdot \mathbf{S}) + A\mathbf{I} \cdot \mathbf{S} + B_{20}O_{20}$$
$$+ B_{22}O_{22} + B_{40}O_{40} + B'_{43}O'_{43}$$

(see main text), where the operator equivalents O_{lm} are referred to a Cartesian coordinate system fixed at the Mn^{2+} site. The axes are the principal axes of the O_{20} and O_{22} contribution to the crystalline electric field (see text). The operator O'_{43} is referred to a Cartesian coordinate system associated with a site in calcite below the transformation. Specifically, the standard operators can be written as follows (see Abragam and Bleaney[11]):

$$\mathbf{H} \cdot \overleftrightarrow{g} \cdot \mathbf{S} = gHS_z \cos\theta + \tfrac{1}{2}gH \sin\theta(S_- e^{i\phi} + S_+ e^{-i\phi})$$

(where the g tensor is taken to be scalar),

$$\mathbf{I} \cdot \mathbf{S} = I_z S_z + \tfrac{1}{2}(I_+ S_- + I_- S_+) ,$$

$$O_{20} = 3S_z^2 - S(S+1) ,$$

$$O_{22} = \tfrac{1}{2}(S_+^2 + S_-^2) ,$$

$$O_{40} = 35S_z^4 - 30S(S+1)S_z^2 + 25S_z^2$$
$$- 6S(S+1) + 3S^2(S+1)^2 ,$$

$$O'_{43} = \tfrac{1}{4}[S_{z'}(S_{+'}^3 + S_{-'}^3) + (S_{+'}^3 + S_{-'}^3)S_{z'}] .$$

The free-ion eigenvectors $|Sm_s Im_I\rangle$ are used to calculate the matrix elements and to carry out the energy calculations. The hyperfine interaction term $A\mathbf{I} \cdot \mathbf{S}$ is ignored for the angular-dependence calculations as justified below. The 6×6 matrices for the spin Hamiltonian (less hyperfine term) in the $|Sm_s\rangle$ basis are (exclusive of the O_{43} term):

m_s \ $m_{s'}$	$\frac{5}{2}$	$\frac{3}{2}$	$\frac{1}{2}$	$-\frac{1}{2}$	$-\frac{3}{2}$	$-\frac{5}{2}$
$\frac{5}{2}$	H_{11}	H_{12}	H_{13}	O	O	O
$\frac{3}{2}$	H_{12}^*	H_{22}	H_{23}	H_{24}	O	O
$\frac{1}{2}$	H_{13}	H_{23}^*	H_{33}	H_{34}	H_{24}	O
$-\frac{1}{2}$	O	H_{24}	H_{34}^*	H_{44}	H_{23}	H_{13}
$-\frac{3}{2}$	O	O	H_{24}	H_{23}^*	H_{55}	H_{12}
$-\frac{5}{2}$	O	O	O	H_{13}	H_{12}^*	H_{66}

where

$$H_{11} = \tfrac{5}{2}g\beta H \cos\theta + 60B_{40} + 10B_{20} ,$$

$$H_{22} = \tfrac{3}{2}g\beta H \cos\theta - 180B_{40} - 2B_{20} ,$$

$$H_{33} = \tfrac{1}{2}g\beta H \cos\theta + 120B_{40} - 8B_{20} ,$$

$$H_{44} = -\tfrac{1}{2}g\beta H \cos\theta + 120B_{40} - 8B_{20} \, ,$$

$$H_{55} = -\tfrac{3}{2}g\beta H \cos\theta - 180B_{40} - 2B_{20} \, ,$$

$$H_{66} = -\tfrac{5}{2}g\beta H \cos\theta + 60B_{40} + 10B_{20} \, ,$$

$$H_{12} = \frac{\sqrt{5}}{2}g\beta H \sin\theta e^{-i\phi} \, ,$$

$$H_{13} = \sqrt{10}B_{22} \, ,$$

$$H_{23} = \sqrt{2}g\beta H \sin\theta e^{-i\phi} \, ,$$

$$H_{24} = 3\sqrt{2}B_{22} \, ,$$

$$H_{34} = \tfrac{3}{2}g\beta H \sin\theta e^{-i\phi} \, .$$

The O'_{43} operator is written with respect to the calcite-site axes rather than the CaCO$_3$(II)-site axes. In the CaCO$_3$(II)-site axes the operator

$$O_{43} = R^{\dagger}[-\psi,-\theta,(-\phi+\lambda)]O'_{43}R[-\psi,-\theta,(-\phi-\lambda)]$$

has the matrix, $\langle m_s \mid O_{43} \mid m'_s \rangle$:

$m_s \backslash m'_s$	$\frac{5}{2}$	$\frac{3}{2}$	$\frac{1}{2}$	$-\frac{1}{2}$	$-\frac{3}{2}$	$-\frac{5}{2}$
$\frac{5}{2}$	O	O	O	$3\sqrt{10}$	O	O
$\frac{3}{2}$	O	O	O	O	O	O
$\frac{1}{2}$	O	O	O	O	O	$-3\sqrt{10}$
$-\frac{1}{2}$	$3\sqrt{10}$	O	O	O	O	O
$-\frac{3}{2}$	O	O	O	O	O	O
$-\frac{5}{2}$	O	O	$-3\sqrt{10}$	O	O	O

The rotation operator R from the CaCO$_3$(II)-site-2 axis to the calcite site-2 axis is

$$R[-\psi,-\theta,(-\phi+\lambda)] = e^{+i\psi S_z}e^{+i\theta S_x}e^{+i(\phi-\lambda)S_z} \, ,$$

where ϕ, θ, ψ are the Euler angles shown in Fig. 2 of the main text through which the crystal reference axes are rotated into the CaCO$_3$(II) site-2 axes, and λ is the angle (15.5°) the calcite-site-2 axes are rotated from the crystal reference axes. For site (1), the angles ϕ, θ, ψ, and λ have opposite signs. This rotation is carried out explicitly only numerically (i.e., by computer) for the Euler angles of interest.

It should be noted that the 6×6 matrices are, in general, complex: $H = R + iI$. The eigenvalues of this matrix can be shown to be the same as those of the 12×12 matrix: $\begin{pmatrix} R & I \\ -I & R \end{pmatrix}$ which is real. The eigenvalues of this real Hamiltonian matrix, and, consequently, the energy levels of the CaCO$_3$(II):Mn^{2+} system, are found using a standard computer code. The eigenvalues for neighboring values of m_s are then subtracted and the differences compared with $h\nu$, the energy of the microwave photons. In this way the magnetic field values, $H_{\text{transition}}$, are found which correspond to the five EPR transitions (without hyperfine interaction). The matrix diagonalization is carried ried out every 50 G in the range of the magnetic resonance spectrum, with a linear interpolation used between these values. This simplfied problem for which the hyperfine interaction is dropped is used to calculate the theoretical angular dependence of the magnetic resonance signals. The foregoing matrix diagonalization process is carried out for increasing values of the polar angle and/or the azimuthal angle and a smooth curve of $H_{\text{transition}}$ versus angle is plotted.

In order to calculate the hyperfine-interaction effects, the full 36×36 matrix is diagonalized for only those angles at which the matrix can be made real: in the x-z plane with a variable polar angle or in the x-y plane with a variable azimuthal angle. Inasmuch as the 36×36 matrix diagonalization is expensive in computer time and, furthermore, the hyperfine interaction is expected not to depend upon orientation of the magnetic field, the full matrix diagonalization is carried out for only the orientations of magnetic field, along the z_2 and y_2 axes. These results are given in Table II of the main text.

---

*Present address: Department of Physics and Atmospheric Science, Drexel University, Philadelphia, PA 19104.

[1]P. W. Bridgman, Am. J. Sci. 237, 7 (1939).

[2]A. Van Valkenburg, Appl. Opt. 9, 1 (1970).

[3]L. Merrill and W. A. Bassett, Acta Crystallogr. B 31, 343 (1975).

[4]L. Merrill, in Proceedings of the 4th International Conference on High Pressure, AIRAPT, Kyoto, Japan, edited by J. Osugi (Kawa Kita, Kyoto, 1975), pp. 389–392.

[5]K. A. Müller, W. Berlinger, and F. Waldner, Phys. Rev. Lett. 21, 814 (1968).

[6]A. Müller, in Structural Phase Transitions and Soft Modes, edited by Emil J. Samuelsen, Eigil Anderson, and Jens Feder (Universitetsforlaget, Oslo, 1971), pp. 61–95.

[7]F. K. Hurd, M. Sachs, and W. D. Hershberger, Phys. Rev. 93, 373 (1954).

[8]C. Kikuchi, Phys. Rev. 100, 1243 (1955).

[9]H. M. McConnell, J. Chem. Phys. 24, 904 (1956).

[10]G. E. Barberis, R. Calvo, H. G. Maldonado, and C. E. Zarote, Phys. Rev. B 12, 853 (1975).

[11]The directions for the crystal-field site x axis shown in Fig. 1 are those given by Barberis et al. but are shown on opposite sites than given by those authors in Fig. 3 of their paper. We are confident a transposition error was made by them.

[12]A. Abragam and B. Bleaney, Electron Paramagnetic Resonance of Transition Ions (Clarendon, Oxford, 1970), Chap. 3.

[13]J. D. Barnett, S. D. Tyagi, and H. M. Nelson, Rev. Sci. Instrum. 49, 348 (1978).

[14]J. D. Barnett, S. Block, and G. J. Piermarini, Rev. Sci. Instrum. 44, 1 (1973).

[15]L. Merrill (private communication).

[16]D. M. Hatch and L. Merrill, Phys. Rev. B 23, 368 (1981).

[17]Jeffrey W. Felix, Ph.D thesis, Brigham Young University, 1984 (unpublished).

[18]J. W. Felix and D. M. Hatch, Phys. Rev. Lett. 53, 2425 (1984).